JOURNAL OF GUIDANCE, CONTROL, AND DYNAMICS
Vol. 33, No. 2, March–April 2010

Electrostatic Spacecraft Collision Avoidance Using Piecewise-Constant Charges

Shuquan Wang* and Hanspeter Schaub†
University of Colorado, Boulder, Colorado 80302

DOI: 10.2514/1.44397

This paper develops a three-phase piecewise-constant spacecraft charge maneuver to achieve short-range collision avoidance with a symmetric relative trajectory. This symmetric trajectory guarantees collision avoidance, restores the original relative-motion direction, and keeps the relative kinetic energy level the same as the initial kinetic energy level. The paper first presents an analytical solution to calculate a unique symmetric trajectory when the middle phase is a circular trajectory. Next, a general symmetric-trajectory programming strategy is developed in which the middle phase can be any conic section. Four constraints are required to guarantee a symmetric collision-avoidance trajectory, and five independent variables are required to solve the problem. This leaves one degree of freedom that is used to optimize the trajectory subject to specific cost charge functions. There is a duality in the charge solution when solving for the open-loop trajectory, with one of the solutions being false. This is addressed by properly initializing and confining the region of the numerical search routine. Minimum charge criteria are determined to avoid a collision by analyzing the geometric properties of the two-body system and comparing the results from circular transitional trajectory calculations.

I. Introduction

CLUSTERED spacecraft have many advantages over a single large monolithic satellite. However, spacecraft cluster concepts also introduce the issue of potential collisions. In close-proximity spacecraft missions, such as close formations and small satellite swarms, the chance for spacecraft to collide must be treated carefully to prevent the huge cost of an unexpected collision. Collisions can occur when some spacecraft within the cluster have control or sensor failures or are lacking in their guidance strategy to guarantee collision avoidance among a large number of cluster members. For long-term formation-flying missions, a collision can also occur when the influences of the orbital disturbances accumulate. The chance of a potential collision from multiple sources motivates the studies of the spacecraft collision-avoidance problem.

The most common approach in dealing with spacecraft collision avoidance is to examine the collision probability of a spacecraft cluster and to perform some velocity corrections to reduce the probability to an acceptable level. Patera and Peterson [1] develop a method to select a maneuver that will reduce the collision probability. This method minimizes the maneuver magnitude and space vehicle propellant expenses. Slater et al. [2] use the available state and disturbance information to calculate the actual probability of collision based on a probabilistic model, then discuss the velocity correction requirements to avoid collisions. Patera [3] proposes a spherical conflict volume to calculate the conflict probability in identifying high-risk conjunctions. The conflict probabilities are larger than associated collision probabilities and therefore are more easily interpreted. All of the above works use thrusters to achieve the velocity corrections. These strategies use propellent, which will increase the fuel budget of the spacecraft. Further, the associated exhaust-plume impingement may cause damage to the instruments onboard in a close-proximity formation.

In this paper, a different scenario is considered, in which an active coulomb control strategy is used after a potential collision has been detected. The craft are assumed to be moving within dozens of meters from each other, and the relative velocities are small: on the order of centimeters per second. This collision-avoidance strategy is not applicable to rapidly approaching spacecraft because of the technical challenges of achieving sufficiently large electrostatic fields. Instead, this work assumes fields that are comparable with the electrostatic potentials that can occur naturally with geostationary spacecraft. Here, the potentials can reach multiple kilovolt levels [4]. The collision-avoidance maneuver strategy uses only piecewise-constant electrostatic (coulomb) forces. Coulomb thrusting can generate the required micro- and millinewton levels of forces to avoid a collision of two slowly drifting spacecraft while requiring essentially no propellant and a few watts of electrical power.

The concept of coulomb thrusting or coulomb formation flying (CFF) was first introduced by King et al. [4]. CFF uses coulomb forces to control the distances between spacecraft to achieve the desired relative motion. Spacecraft will naturally charge to either positive or negative voltages, due to their interaction with the local space-plasma environment. The spacecraft charge level can be actively controlled by continuously emitting electrons or ions, as performed on the current Cluster mission [5,6]. The fuel efficiency of coulomb thrusting is at least three–five orders greater than that of electric propulsion and typically requires only a few watts of electrical power to operate [4]. A challenge of CFF is that, unlike conventional thrusters that can produce a thrust vector in any direction, the coulomb forces lie only along the line-of-sight directions between spacecraft. But this is less of an issue when using coulomb forces to avoid a collision. The most important factor in preventing collision is the separation distance, which can be fully controlled using coulomb forces. Another challenge of CFF is that the sparse space plasma will shield electrostatic charges. This effect will reduce the amount of electrostatic force that a neighboring charged spacecraft will experience. The amount of shielding is characterized by the Debye length [7,8]. At separation distances greater than a Debye length, the perceived intercraft coulomb force quickly becomes negligible. At low Earth orbits, in which the plasma is relatively dense and cold, the Debye length is on the order of centimeters. This results in a strong shielding of coulomb forces and makes coulomb thrusting not feasible. However, at geosynchronous Earth orbits (GEO), the Debye lengths range between 100–1000 m

Presented at the 19th AAS/AIAA Space Flight Mechanics Meeting, Savannah, GA, 8–12 February 2009; received 23 March 2009; revision received 5 October 2009; accepted for publication 5 October 2009.

*Graduate Research Assistant, Aerospace Engineering Sciences Department. Student Member AIAA.

†Associate Professor, Aerospace Engineering Sciences Department. Associate Fellow AIAA.

[4,9]. At 1 AU in deep space the Debye length ranges around 20–50 m [4]. This makes the coulomb-thrusting concept feasible for high Earth orbits and deep-space missions when the minimum separation distances are less than 100 m.

The CFF concept has been investigated for several different mission scenarios. Lappas et al. [10] develop a hybrid propulsion strategy by combining coulomb forces and standard electric thrusters for formation flying on the orders of tens of meters in GEO. Shaub and Hussein [11] analyze the stability of a spinning two-craft coulomb tether and show that if the Debye length is larger than the separation distance, then the nonlinear radial motion is locally stable; otherwise, the radial motion is unstable. The perturbed out-of-plane motion is always stable, regardless of Debye length. Vasavada and Schaub [12] present analytical tools to determine the charge solution for a static four-craft formation. Wang and Schaub [13] design a two-stage charge feedback-control strategy for a 1-D constrained coulomb structure and analyze the condition for symmetric relative motions of coulomb structure to be stabilizable by investigating the total energy of the system. Hussein and Schaub [14] derive the collinear three-craft spinning family of solutions. Feedback control based on the linearized model is designed to stabilize a collinear virtual coulomb tether system. Asymptotic stability is achieved if the system's angular momentum is equivalent to the estimated/nominal angular momentum, which is used to calculate the nominal charges. However, none of these CFF-related works consider the issue of performing active collision avoidance. Such a capability will be required when considering flying larger numbers of craft in close proximity.

Reference [15] is the first publication that develops a collision-avoidance strategy using only coulomb forces. A controller is designed based on Lyapunov stability analysis and requires only feedback on separation distance. Without charge saturations, the controller can prevent any collision. Considering charge saturations, the paper finds the analytical criteria for an avoidable collision by assuming the Debye length to be infinity. Although this feedback-control strategy can maintain specified safety separation distances, this control will cause the craft to depart in a different direction from when the collision-avoidance maneuver started. This change in direction should be avoided if possible, to not redirect the craft and cause them to approach another craft.

Instead of designing a feedback-control strategy, this paper investigates an open-loop strategy to find a symmetric trajectory to achieve the collision-avoidance objective. In particular, a solution is sought that retains the original relative velocity vector after the collision-avoidance maneuver. The paper investigates how to develop such open-loop charged relative-motion trajectories. How to feedback-stabilize such a trajectory and make it robust to unmodeled dynamics and sensor errors is the topic of future work. Such a feedback strategy is nontrivial, due to the underactuated nature of the coulomb force. For example, the line-of-sight force cannot change the momentum vector to reverse an overshoot. Assuming the Debye length to be large compared with the separation distance and assuming that the spacecraft charges are piecewise-constant, the relative equations of motion during a constant charge phase have exactly the same algebraic form as in the gravitational two-body problem (G2BP). In this work, the spacecraft are assumed to be operating in deep space and not orbiting a gravitational body. Thus, the relative-trajectory segments corresponding to constant spacecraft charge result in conic sections [16]. By switching the spacecraft charges, a symmetric trajectory made of three patched conic sections, repel–attract–repel, is sought to achieve a collision avoidance meanwhile to retain the relative-speed magnitude and direction. The geometries of the symmetric trajectories are explored to investigate charge optimality of the resulting open-loop maneuvers. This is important when the limited charge capability of an actual craft is taken into consideration. Further, given a maximum charging capability, initial condition criteria that lead to a successful collision-avoidance maneuver are explored.

II. Problem Statement

A. Charged Spacecraft Equations of Motion

This paper considers two-spacecraft free-flying in three-dimensional space in which there are no external forces acting on the system. The scenario of the two-body system is shown in Fig. 1. Assuming point-charge models for the spacecraft, the partially shielded electrostatic potential generated by the ith spacecraft in a plasma environment is given by [17]

$$V_i(r) = k_c \frac{q_i}{r} \exp(-r/\lambda_d) \tag{1}$$

where $k_c = 8.99 \times 10^9\ \mathrm{C}^{-2} \cdot \mathrm{N} \cdot \mathrm{m}^2$ is the coulomb constant, q_i is the charge of the ith spacecraft, r is the separation distance between the ith spacecraft and point of interest, and λ_d is the Debye length that characterizes the strength of the plasma shielding effect. The corresponding electrostatic field is obtained by taking the gradient of the potential:

$$E_i(\boldsymbol{r}) = -\nabla_{\boldsymbol{r}} V_i(r) = k_c \frac{q_i}{r^2}\left(1 + \frac{r}{\lambda_d}\right)\exp\left(-\frac{r}{\lambda_d}\right)\hat{\boldsymbol{e}}_r \tag{2}$$

where $\boldsymbol{r}$ is the inertial position vector pointing from the ith spacecraft to point of interest, and $\hat{\boldsymbol{e}}_r$ is the unit vector of $\boldsymbol{r}$. Thus, the coulomb force between the two spacecraft, acting on m_1, is

$$\begin{aligned}\boldsymbol{F} &= q_1 E_2(\boldsymbol{r}_{21}) = k_c \frac{q_1 q_2}{r^2}\left(1 + \frac{r}{\lambda_d}\right)\exp\left(-\frac{r}{\lambda_d}\right)\hat{\boldsymbol{e}}_{21} \\ &= -k_c \frac{q_1 q_2}{r^2}\left(1 + \frac{r}{\lambda_d}\right)\exp\left(-\frac{r}{\lambda_d}\right)\hat{\boldsymbol{e}}_{12}\end{aligned} \tag{3}$$

where $\boldsymbol{r}_{12}$ is the relative position vector from spacecraft 1 (SC1) to spacecraft 2 (SC2), and $\hat{\boldsymbol{e}}_{12}$ is the unit vector of $\boldsymbol{r}_{12}$. In the remaining context, we use $\hat{\boldsymbol{e}}_r$ to represent $\hat{\boldsymbol{e}}_{12}$ for brief notation. From the expression of the coulomb force, it can be seen that the smaller the plasma Debye length, the shorter the effective range of a given electrical charge. For high Earth orbits, the Debye length ranges between 100 and 1000 m [4,18,19]. In deep space at 1 AU (astronomical unit) distance from the sun, the Debye length can vary between 30–50 m. CFF typically has spacecraft separation distances less than 100 m.

The inertial equations of motion (EOM) of the two charged spacecraft are

$$m_1 \ddot{\boldsymbol{R}}_1 = -k_c \frac{q_1 q_2}{r^2}\left(1 + \frac{r}{\lambda_d}\right)\exp\left(-\frac{r}{\lambda_d}\right)\hat{\boldsymbol{e}}_r \tag{4a}$$

$$m_2 \ddot{\boldsymbol{R}}_2 = k_c \frac{q_1 q_2}{r^2}\left(1 + \frac{r}{\lambda_d}\right)\exp\left(-\frac{r}{\lambda_d}\right)\hat{\boldsymbol{e}}_r \tag{4b}$$

where $\boldsymbol{R}_i$ is the inertial position vector of the ith spacecraft. The inertial relative acceleration vector $\ddot{\boldsymbol{r}}$ is

$$\ddot{\boldsymbol{r}} = \ddot{\boldsymbol{R}}_2 - \ddot{\boldsymbol{R}}_1 = \frac{k_c q_1 q_2}{m_1 m_2 r^2}(m_1 + m_2)\left(1 + \frac{r}{\lambda_d}\right)\exp\left(-\frac{r}{\lambda_d}\right)\hat{\boldsymbol{e}}_r \tag{5}$$

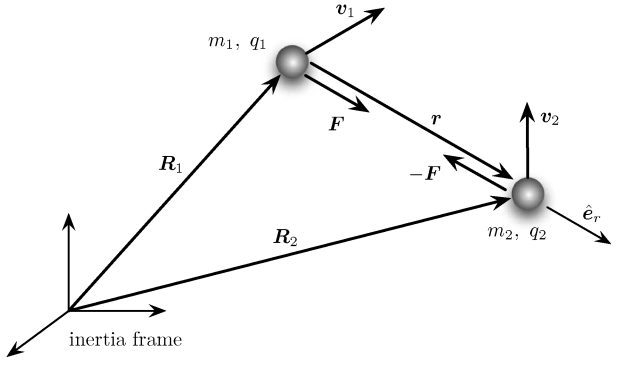

Fig. 1 Illustration of the two-spacecraft system.

Note that these equations do not explicitly consider planetary gravity and the Lorentz forces acting on the spacecraft. Pollock et al. [19] prove that the Lorentz-force magnitude is not comparable with the coulomb force in GEO. If the collision-avoidance maneuver time is very small compared with the cluster orbital period, then Eq. (5) can also be considered as an approximation of the charged relative orbital motion. For example, a GEO spacecraft collision-avoidance maneuver that takes minutes would be very short compared with the one-day orbit period, and thus the relative orbital motion would have a secondary effect on the relative motion.

This paper finds a symmetric patched-conic-section trajectory to prevent a collision, while forcing the departure velocity vector to be the same as the initial arrival velocity vector. Hussein and Schaub [16] show that if $\lambda_d \to \infty$ and the charge product $Q = q_1 q_2$ is constant, then the relative-motion trajectory of the two spacecraft is a conic section. Letting $\lambda_d \to \infty$ and defining

$$\mu = -k_c \frac{Q(m_1 + m_2)}{m_1 m_2} \tag{6}$$

Eq. (5) is rewritten as

$$\ddot{\boldsymbol{r}} = -\frac{\mu}{r^3}\boldsymbol{r} \tag{7}$$

Equation (7) has exactly the same algebraic form as the EOM of the G2BP. If the charge product Q is constant, then the effective gravitational coefficient μ is also constant. Thus, the resulting motion can be described by a conic section. Note that μ can be positive or negative here. The negative and constant charge product results in a positive effective gravitational constant $\mu > 0$. In this case, Eq. (7) is exactly the same as the G2BP. If Q is negative and constant, then the relative trajectory is a repulsive hyperbola, in which SC2 is moving along a hyperbola and SC1 stays at the farther focus point [16]. If the charge product Q is piecewise-constant, then the relative trajectory would be a patched conic section.

B. Three-Phase Symmetric-Trajectory Scenario

For a two-spacecraft system controlled only by coulomb forces, there is generally an infinity of possible charge and charge switching-time solutions that achieve a collision avoidance. This paper investigates a symmetric-trajectory programming approach to avoid a collision as well as to hold the relative velocity.

An example of the symmetric relative-trajectory scenario is shown in Fig. 2. The controlled part of the symmetric trajectory is composed of three phases: repel–attract–repel. At the beginning, the two spacecraft are flying freely and approaching each other such that their minimum separation distance will violate a desired safety distance r_s. At point A, the separation distance r between the spacecraft reaches a potential collision region range r_ϕ. The spacecraft are charged such that $Q > 0$ and the spacecraft start to repel each other to avoid the collision. The magnitude of the charge product is held constant in phase I until point B is reached. Thus, the trajectory $\widehat{AB}$ is a repulsive hyperbola. At point B, the charge product switches to a negative value such that the spacecraft are attracting each other. During phase II from point B to point C, the charge product is again held constant. The arc $\widehat{BC}$ is an attractive conic section that can be ellipsis, parabola, or hyperbola, depending on the relative arrival velocity magnitude. At point C, the charge product switches back to the same value as in arc $\widehat{AB}$ to produce a symmetric trajectory to $\widehat{AB}$. At point E, the spacecraft are discharged and begin to fly freely in space. The entire trajectory is symmetric about the axis $\overline{OD}$. The symmetry axis $\overline{OD}$ is the line crossing SC1 and perpendicular to the initial relative velocity.

From the above description of the three-phase trajectory, it can be seen that the trajectory is determined by the three-charge product during the three phases and by the two-charge switching time at points B and C. Once these five variables are determined, the relative trajectory is determined.

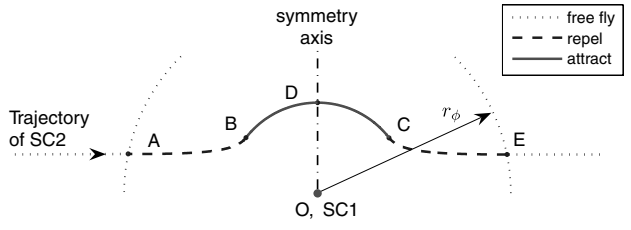

Fig. 2 Illustration of the symmetric patched-conic-section trajectory with respect to SC1.

III. Circular Transitional Orbit Programming

Before studying the general symmetric trajectories, let us first investigate a special case in which the phase II trajectory is a section of a circle, as illustrated in Fig. 3. Assume that the relative position vector $\boldsymbol{r}_A$ and the relative velocity $\dot{\boldsymbol{r}}_A$ at point A can be measured. There are five unknown parameters that need to be determined: the three charge products $Q_{\rm I}$, $Q_{\rm II}$, and $Q_{\rm III}$ and the two-charge switching times at points B and C. To solve for these five variables, some constraints must be clarified.

A. Constraints

For phase I $\widehat{AB}$ and phase III $\widehat{CE}$ to be symmetric, the charge products should be the same value. Thus, the first constraint is

$$Q_{\rm III} = Q_{\rm I} \tag{8}$$

Because the trajectory of phase II $\widehat{BC}$ is a section of a circle, its shape is always symmetric about the symmetry axis $\overline{OD}$. Then a symmetric arc $\widehat{BC}$ requires that the angle $\angle DOC$ satisfies

$$\angle DOC = \angle BOD \tag{9}$$

Point B connects phase I and phase II. Thus, $\dot{\boldsymbol{r}}_B$ must be perpendicular to $\boldsymbol{r}_B$ because phase II is circular. This implies that point B is the periapsis of phase I. This results in the third constraint:

$$r_B = r_{p\rm I} \tag{10}$$

The trajectory of phase II is a section of a circle; this requirement can be formulated using the angular momentum magnitude:

$$h_{\rm II}^2 = \mu_{\rm II} r_B \tag{11}$$

The collision-avoidance task requires that the separation distance $r(t)$ must be greater than a certain safe-restraint distance r_s for all time:

$$r(t) \geq r_s \tag{12}$$

This constraint is global and comes from the collision-avoidance mission. For the convenience of calculation, this safety constraint is expressed by the condition

$$r_{\min} = \gamma r_s \tag{13}$$

where $\gamma \geq 1$. In the case in which phase II is a section of a circle, $r_{\min} = r_B$. Thus, the final safety constraint for a circular transitional symmetric trajectory is

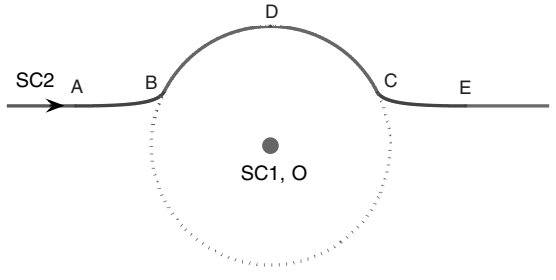

Fig. 3 Scenario of the circular phase II trajectory.

$$r_B = \gamma r_s \tag{14}$$

Now five constraints given in Eqs. (8–11) and (14) have been found.

B. Circular Transitional Orbit Algorithm

The symmetric constraint in Eq. (8) provides Q_{III} once Q_{I} is obtained. Note that the angle $\angle DOC$ is the true anomaly angle (in case point D is the periapsis) of phase II. Once the conic-section properties of phase II, which are determined by Q_{II}, are achieved, the charge switching time at point C is then solved by using Kepler's equation and the symmetry constraint in Eq. (9).

Now there are three variables $(Q_{\mathrm{I}}, Q_{\mathrm{II}}, t_{\mathrm{I}})$ left out of the five unknown parameters that still need to be determined. The conic-section properties of phase I are solved using $\boldsymbol{r}_A$ and $\dot{\boldsymbol{r}}_A$. The eccentricity vector of phase I is

$$\boldsymbol{c}_{\mathrm{I}} = \dot{\boldsymbol{r}}_A \times \boldsymbol{h} - \frac{\mu_{\mathrm{I}}}{r_A}\boldsymbol{r}_A \tag{15}$$

where $r_A = |\boldsymbol{r}_A|$, $\boldsymbol{h} = \boldsymbol{r}_A \times \dot{\boldsymbol{r}}_A$ is the specific angular momentum of the system, and

$$\mu_{\mathrm{I}} = -k_c \frac{Q_{\mathrm{I}}(m_1 + m_2)}{m_1 m_2} \tag{16}$$

is the effective gravitational coefficient of phase I. Note that, through Eq. (6), finding the charge products Q_{I} and Q_{II} is equivalent to finding μ_{I} and μ_{II}. The vector $\boldsymbol{h}$ is constant by the assumption that there are no external forces acting on the system. The eccentricity and semimajor axis of phase I are calculated by

$$e_{\mathrm{I}} = -\frac{\|\boldsymbol{c}_{\mathrm{I}}\|}{\mu_{\mathrm{I}}} \tag{17a}$$

$$a_{\mathrm{I}} = \frac{r_A \mu_{\mathrm{I}}}{2\mu_{\mathrm{I}} - r_A v_A^2} \tag{17b}$$

where $v_A = \|\dot{\boldsymbol{r}}_A\|$ is the magnitude of the relative velocity vector. The angle $\angle AOD$ is calculated as

$$\angle AOD = \arctan\left(\frac{h}{r_A v_A}\right) - \frac{\pi}{2} \tag{18}$$

Using the constraint that point B must be the periapsis of phase I, the charge switching time t_B at point B is calculated via

$$t_B = \frac{|N_{AI}|}{\sqrt{\mu_{\mathrm{I}}/a_{\mathrm{I}}}} \tag{19}$$

with the right-hand side of this equation being completely determined by μ_{I}, which in return is determined by Q_{I}. Thus, it can be concluded that the phase I trajectory is determined by the charge product Q_{I}.

The radius r_B is calculated by

$$r_B = \frac{h^2/\mu_{\mathrm{I}}}{1 - e_{\mathrm{I}}} \tag{20}$$

where the eccentricity e_{I} is given by Eq. (17a). Substituting Eq. (20) into the safety constraint in Eq. (14) and multiplying both sides by $\mu_{\mathrm{I}}(1 - e_{\mathrm{I}})/(\gamma r_s)$ yields

$$\mu_{\mathrm{I}}(1 - e_{\mathrm{I}}) = \frac{h^2}{\gamma r_s} \tag{21}$$

Subtracting both sides by μ_{I}, taking the square of both sides, and using

$$e_{\mathrm{I}} = -\frac{\|\boldsymbol{c}\|}{\mu_{\mathrm{I}}} = \left\| \frac{\boldsymbol{r}_A}{r_A} - \frac{\dot{\boldsymbol{r}}_A \times \boldsymbol{h}}{\mu_{\mathrm{I}}} \right\|$$

yields

$$\mu_{\mathrm{I}}^2 e_{\mathrm{I}}^2 = \mu_{\mathrm{I}}^2 - 2\mu_{\mathrm{I}} \dot{\boldsymbol{r}}_A \times \boldsymbol{h} \cdot \boldsymbol{r}_A / r_A + \dot{\boldsymbol{r}}_A \times \boldsymbol{h} \cdot \dot{\boldsymbol{r}}_A \times \boldsymbol{h} \tag{22}$$

Substituting Eq. (22) into Eq. (21) yields

$$-2\mu_{\mathrm{I}} \dot{\boldsymbol{r}}_A \times \frac{\boldsymbol{h} \cdot \boldsymbol{r}_A}{r_A} + \dot{\boldsymbol{r}}_A \times \boldsymbol{h} \cdot \dot{\boldsymbol{r}}_A \times \boldsymbol{h} = \frac{h^4}{\gamma^2 r_s^2} - \frac{2\mu_{\mathrm{I}} h^2}{\gamma r_s} \tag{23}$$

Thus, the phase I effective gravitational coefficient for a circular transitional trajectory is solved by grouping terms containing μ_{I}:

$$\mu_{\mathrm{I},c} = \frac{1}{2} \frac{\frac{h^4}{\gamma^2 r_s^2} - \dot{\boldsymbol{r}}_A \times \boldsymbol{h} \cdot \dot{\boldsymbol{r}}_A \times \boldsymbol{h}}{\frac{h^2}{\gamma r_s} - \dot{\boldsymbol{r}}_A \times \boldsymbol{h} \cdot \frac{\boldsymbol{r}_A}{r_A}} \tag{24}$$

After obtaining $\mu_{\mathrm{I},c}$, the variable t_{I} is determined by Eq. (19). These values of μ_{I} and t_{I} ensure that at point B the relative-speed vector is perpendicular to the relative position vector; meanwhile, the safety constraint $r_B = \gamma r_s$ is also satisfied.

The next step is to find a proper Q_{II} or μ_{II} that results in a circular orbit. Using the constraint for a circular transitional orbit in Eq. (11), μ_{II} is found to be

$$\mu_{\mathrm{II},c} = \frac{h^2}{r_B} = \frac{h^2}{\gamma r_s} \tag{25}$$

To find the phase II duration time t_{II}, the phase II symmetry constraint in Eq. (9) is used. Note that the angular velocity is constant in phase II, the duration time is proportional to the angle $\angle BOC$ as

$$t_{\mathrm{II},c} = \angle BOC \cdot \frac{T_{\mathrm{II}}}{2\pi} = 2\angle BOD \cdot \frac{T_{\mathrm{II}}}{2\pi} = \frac{\angle BOD \cdot T_{\mathrm{II}}}{\pi} \tag{26}$$

where the period of the phase II circular orbit is $T_{\mathrm{II}} = \sqrt{\mu_{\mathrm{II}}/r_{\mathrm{II}}^3}$, and the angle $\angle BOD$ is given by

$$\angle BOD = \angle AOD - |f_{AI}| = \angle AOD + \operatorname{atan}\left(\frac{\hat{\boldsymbol{i}}_{c\mathrm{I}} \times \hat{\boldsymbol{i}}_{rA} \cdot \hat{\boldsymbol{i}}_h}{\hat{\boldsymbol{i}}_{c\mathrm{I}} \cdot \hat{\boldsymbol{i}}_{rA}}\right) \tag{27}$$

where $\hat{\boldsymbol{i}}_{c\mathrm{I}}$, $\hat{\boldsymbol{i}}_{rA}$, and $\hat{\boldsymbol{i}}_h$ are the unit vectors of $\boldsymbol{c}_{\mathrm{I}}$, $\boldsymbol{r}_A$, and $\boldsymbol{h}$, respectively. The angle $\angle AOD$ is expressed in Eq. (18).

Thus, a symmetric trajectory with phase II being a part of a circular orbit has been found. Specifically, the variables μ_{I}, μ_{II}, Q_{III}, t_B, and t_{II} are calculated through Eqs. (24), (25), (8), (19), and (26), respectively. Note that this circular transitional trajectory solution is calculated analytically.

IV. General Symmetric-Trajectory Programming Strategy

After solving a circular phase II trajectory in the last section, this section investigates the more general symmetric collision-avoidance trajectory, with the phase II trajectory being any type of conic section.

A general three-phase symmetric trajectory is shown in Fig. 2. As mentioned in the last section, as with the circular phase II case, there are five unknowns that need to be determined: $[Q_{\mathrm{I}}, Q_{\mathrm{II}}, Q_{\mathrm{III}}, t_B, t_{\mathrm{II}}]$.

A. Constraints

The general constraints are largely the same as those for the circular transitional orbit. The three constraints in Eqs. (8), (9), and (13) are directly used to ensure a symmetric trajectory. Because the phase II trajectory is a part of a general conic section here, the circular constraints in Eqs. (10) and (11) are not applicable.

Since the arc $\widehat{BC}$ does not necessarily have to be a part of a circle, for phase II to be symmetric about the axis $\overline{OD}$, point D must be the periapsis or apoapsis of phase II. This requirement is formulated as

$$r_D = r_{p,\mathrm{II}} \quad \text{or} \quad r_D = r_{a,\mathrm{II}} \tag{28}$$

where $r_{p,\mathrm{II}}$ and $r_{a,\mathrm{II}}$ are the periapsis radius and the apoapsis radius of phase II.

Now there are four equality constraints to solve the patched conic collision-avoidance trajectory. Equations (8), (9), and (28) are from the symmetric patched-conic-section properties and ensure a symmetric trajectory. The constraint given by Eq. (14) is required by the collision-avoidance task. To complete the five-variable searching problem, one more constraint is needed.

Note that the four equality constraints ensure a collision-avoidance trajectory and meanwhile result in a symmetric trajectory. The remaining one degree of freedom actually provides a flexibility in solving for the five variables. This section assumes that a proper value of Q_{I} is given, then constructs a closed-loop numerical iteration routine to find the other four variables. This iteration routine can be used as a part of the charge-optimal trajectory programming algorithm that updates Q_{I} such that a certain charge cost function is minimized. The charge-optimization examples are shown and discussed in the second simulation case in the numerical simulation section.

B. General Numerical Iteration Routine

Assuming that a proper value of Q_{I} has been given, this section develops a numerical iteration routine to find a symmetric patched-conic-section trajectory to avoid a potential collision. The charge product Q_{I} and the initial conditions $[\boldsymbol{r}_A, \dot{\boldsymbol{r}}_A]$ determine the conic section of phase I. Without loss of generality, assume that $t_A = 0$. If t_B is given, the angle $\angle AOB$ can be calculated using Kepler's equation in phase I. The states $[\boldsymbol{r}_B, \dot{\boldsymbol{r}}_B]$ are determined by solving the orbit EOM of phase I. Using the constraint that point D must be the periapsis or apoapsis of phase II, point C is determined by the constraint in Eq. (9). Phase III is determined by the state of point C, which can be inferred from t_B. Thus, the charge switching time t_B logically determines the whole patched-conic-section trajectory. In the numerical iteration routine, t_B is chosen as the variable to be propagated.

Now t_B has been chosen as the variable to be propagated in the iteration loop. Given an initial guess of t_B, it is updated according to the error of a target function. The states at point B are determined by using the conic-section properties of phase I. The mean hyperbolic anomaly of point B considered in phase I is calculated using Kepler's equation:

$$N_{B\mathrm{I}} = N_{A\mathrm{I}} + \sqrt{\frac{\mu_{\mathrm{I}}}{a_{\mathrm{I}}^3}} \cdot t_B = N_{A\mathrm{I}} + n_{\mathrm{I}} \cdot t_B \tag{29}$$

Then the hyperbolic anomaly $H_{B\mathrm{I}}$ is calculated by numerically solving the standard anomaly relationship [20]:

$$N_{B\mathrm{I}} = e_{\mathrm{I}} \sinh(H_{B\mathrm{I}}) + H_{B\mathrm{I}} \tag{30}$$

Thus, the true anomaly of point B in phase I is determined by

$$f_{B,\mathrm{I}} = 2 \cdot \arctan\left(\tanh\left(\frac{H_{B\mathrm{I}}}{2}\right)\sqrt{\frac{e_{\mathrm{I}}+1}{e_{\mathrm{I}}-1}}\right) \tag{31}$$

The radius and the magnitude of the relative velocity at point B are

$$r_B = \frac{h^2/\mu_{\mathrm{I}}}{1 - e_{\mathrm{I}} \cos f_{B\mathrm{I}}} \tag{32a}$$

$$v_B = \sqrt{\mu_{\mathrm{I}}\left(\frac{2}{r_B} - \frac{1}{a_{\mathrm{I}}}\right)} \tag{32b}$$

where h is the magnitude of the specific angular momentum determined by the initial conditions. Equation (32b) is obtained from the energy equation.

After obtaining the relative motion states at point B, phase II is determined by the symmetric conic-section constraints. Specifically, the charge product Q_{II} and point C are determined through the following process. At first, the angle $\angle AOB$ is calculated by

$$\angle AOB = |f_{B,\mathrm{I}} - f_{A,\mathrm{I}}| \tag{33}$$

The angle $\angle BOD$ is determined by the geometry relation:

$$\angle BOD = \angle AOD - \angle AOB \tag{34}$$

According to the symmetric constraint in Eq. (9), the angle

$$\angle COD = \angle BOD \tag{35}$$

is solved. Thus, point C is located. Note that of the five variables that determine the symmetric conic-section trajectory, points B and C and the charge products Q_{I} and Q_{III} have been solved. The only variable left to be determined is the charge product Q_{II}. Solving for μ from Eq. (7) yields

$$\mu_{\mathrm{II}} = -k_c \frac{Q_{\mathrm{II}}(m_1 + m_2)}{m_1 m_2} \tag{36}$$

Once μ_{II} is solved, Q_{II} is also determined. The following development solves for μ_{II} based on the states of point B and the symmetric constraints.

Since the arc $\widehat{BC}$ is a part of a conic section, it has all of the properties of conic-section orbit. Using the vis-viva equation, the eccentricity e is expressed as

$$e = \sqrt{1 + \left(\frac{v^2}{\mu} - \frac{2}{r}\right)\frac{h^2}{\mu}} \tag{37}$$

Because h is assumed to be constant, the expression of the eccentricity in Eq. (37) contains only three unknown variables: r, v, and μ. Substituting Eq. (37) into the radius equation yields

$$r = \frac{h^2}{\mu + \cos f \sqrt{\mu^2 + (v^2 - \frac{2\mu}{r})h^2}} \tag{38}$$

Transforming Eq. (38) to separate the square-root term yields

$$\cos f \sqrt{\mu^2 + \left(v^2 - \frac{2\mu}{r}\right)h^2} = \frac{h^2}{r} - \mu \tag{39}$$

Squaring Eq. (39) and using the fact that $1 - \cos^2 f = \sin^2 f$, Eq. (39) is simplified to be

$$\sin^2 f \mu^2 - \frac{2h^2}{r}\sin^2 f \mu - \cos^2 f v^2 h^2 + \frac{h^4}{r^2} = 0 \tag{40}$$

This equation contains four variables: μ, f, r, and v. Note that Eq. (40) is valid for all conic-section orbits. Evaluating f, r, and v at point B in phase II, Eq. (40) becomes a quadratic equation of μ. The values for r_B and v_B are given by Eq. (32). By the symmetry constraint, point D can only be the periapsis or apoapsis of phase II. If point D is the periapsis, then

$$f_{B,\mathrm{II}} = -\angle BOD \tag{41}$$

Otherwise point D is the apoapsis of phase II with

$$f_{B,\mathrm{II}} = \pi - \angle BOD \tag{42}$$

In both cases, the resulting final equations after substituting $f_{B\mathrm{II}}$ into Eq. (40) are identical:

$$\underbrace{\sin^2\angle BOD}_{l_1}\ \mu_{\mathrm{II}}^2 \underbrace{- \frac{2h^2}{r_B}\sin^2\angle BOD}_{l_2}\ \mu_{\mathrm{II}} \underbrace{- \cos^2\angle BOD v_B^2 h^2 + \frac{h^4}{r_B^2}}_{l_3} = 0 \tag{43}$$

Analytically solving for μ_{II} from Eq. (43), the charge product in phase II is then obtained by Eq. (36).

Note that given μ_{I}, t_B, and $\angle BOD$, there are generally two solutions of μ_{II} to Eq. (43):

$$\mu_{\text{II}}^{(1)} = \frac{h^2}{r_B} + \frac{1}{2\sin^2\angle BOD}\sqrt{l_2^2 - 4l_1 l_3} \tag{44a}$$

$$\mu_{\text{II}}^{(2)} = \frac{h^2}{r_B} - \frac{1}{2\sin^2\angle BOD}\sqrt{l_2^2 - 4l_1 l_3} \tag{44b}$$

Substituting Eq. (44) into the right-hand side (RHS) of Eq. (39) yields

$$\frac{h^2}{r} - \mu = \mp\frac{1}{2\sin^2\angle BOD}\sqrt{l_2^2 - 4l_1 l_3} \tag{45}$$

This indicates that the two solutions result in two opposite signs in the RHS of Eq. (39). But for a particular value of f, either $-\angle BOD$ or $\pi - \angle BOD$, the left-hand side (LHS) of Eq. (39) must has a specific sign. This means that only one of the two solutions to Eq. (43) satisfies Eq. (39). In other words, only one of the two values in Eq. (44) results in a symmetric trajectory.

The plots in Fig. 4 show the two scenarios using $\mu_{\text{II}}^{(1,2)}$ given by Eq. (44). Figure 4a shows the case in which point D is expected to be the periapsis of phase II. Figure 4b shows the case in which point D is designated as the apoapsis of phase II. In Fig. 4a, the angle $\angle BOD = 71.9°$, and $f_{B,\text{II}}$ is expected to be $-\angle BOD = -71.9°$. With this value of $f_{B,\text{II}}$, the LHS of Eq. (39) must be positive. Correspondingly, only $\mu_{\text{II}}^{(2)}$ satisfies Eq. (39). This is confirmed by Fig. 4a. Figure 4b confirms the other case in which only $\mu_{\text{II}}^{(1)}$ results in the symmetric trajectory, with point D being the apoapsis of phase II.

By assuming that the variables Q_{I} and t_B are given, the previous development outlines how to solve for the states at points B and C and the charge product of phase II, Q_{II}. However, in our present algorithm, t_B is not explicitly determined. Note that three constraints have been used in deriving the formulas in Eqs. (8), (28), and (9). The safety constraint in Eq. (13) needs to be implemented to achieve a collision-avoidance trajectory. A numerical search routine is expected to find an appropriate t_B such that the closest distance $r_{\min} = \gamma r_s$, where $\gamma \geq 1$.

The following theorem provides a rule to find the minimum distance in the whole trajectory.

Theorem 1. Consider the three-phase symmetric patched-conic-section trajectory as shown by Fig. 2. If point D is the periapsis of phase II, then the minimum distance of the entire $\widehat{AE}$ trajectory is the periapsis radius of phase II; that is,

$$r_{\min} = r_{p,\text{II}} \tag{46}$$

If point D is the apoapsis of phase II, then the minimum distance is the periapsis radius of phase I; that is,

$$r_{\min} = r_{p,\text{I}} \tag{47}$$

Proof. If point D is the periapsis of phase II, then $r_{p,\text{II}}$ is the minimum distance in phase II. So it is true that $r_{p,\text{II}} < r_B$. Because $\angle BOD < 90°$ and $f_{B,\text{II}} \in (-90, 0°)$, thus $\dot{r}_B < 0$. Then the periapsis of phase I does not lie along the arc $\widehat{AB}$. This indicates that throughout phase I, $\dot{r} < 0$. Thus, r_B is the minimum distance in phase I. Because $r_{p,\text{II}} < r_B$, the minimum distance in the entire trajectory is $r_{p,\text{II}}$.

If point D is the apoapsis of phase II, then r_B is the minimum distance in phase II, because $f_{B,\text{II}} \in (90, 180°)$ and $\dot{r}_B > 0$. Note that if $\dot{r}_A < 0$, then the periapsis of phase I must lie in the arc $\widehat{AB}$, because $\dot{r}$ crosses zero in phase I. So $r_{p,\text{I}}$ is the minimum distance in phase I, which indicates that $r_{p,\text{I}} < r_B$. Because r_B is the minimum distance in phase II, the minimum distance in the entire trajectory $r_{p,\text{I}}$. □

The proof of Theorem 1 indicates that if point D is the periapsis of phase II, then $t_B < t_{p,\text{I}}$, where $t_{p,\text{I}}$ is the time for SC2 to fly from point A to the periapsis of phase I. If point D is the apoapsis of phase II, then $t_B > t_{p,\text{I}}$. Figure 5b illustrates this scenario in detail. Figure 6 shows the change of $r_{p,\text{II}}$ with respect to t_B, assuming that μ_{I} is fixed. It can be seen that when $t_B < t_{p,\text{I}}$ and $\mu_{\text{II}}^{(2)}$ is used, $r_{p,\text{II}}$ is monotonically increasing as t_B increases; when $t_B > t_{p,\text{I}}$ and $\mu_{\text{II}}^{(1)}$ is used, $r_{p,\text{II}}$ is monotonically decreasing as t_B increases. Thus, a symmetric collision-avoidance trajectory with point D being the periapsis of phase II can be solved by initializing $t_B^{(0)} < t_{p,\text{I}}$ and updating t_B using common numerical methods such as Newton's method or the secant method.

Alternatively initializing $t_B^{(0)} > t_{p,\text{I}}$ and using $\mu_{\text{II}}^{(1)}$ lead to a symmetric collision-avoidance trajectory with point D being the apoapsis of phase II. In this case, by setting $r_{p,\text{I}} = \gamma r_s$ and solving for corresponding μ_{I} from Eq. (24), any symmetric solution of phase II trajectory will satisfy the collision-avoidance requirement. Thus, there are infinite choices of t_B that lead to symmetric maneuvers if point D is the apoapsis of phase II.

Before performing a numerical search for t_B under a given μ_{I}, it must be decided a priori whether a periapsis or an apoapsis point D solution is being sought. During the numerical iterations the current estimates of t_B must be constrained to remain either larger or smaller than $t_{p,\text{I}}$. If t_B crosses $t_{p,\text{I}}$ without switching the μ_{II} solution, the algorithm will lead to an asymmetric trajectory with $f_{B,\text{II}}$ lying in a wrong quadrant, as shown by the dashed lines in Fig. 4.

Note that the path with point D being the apoapsis of phase II is a longer path, both in length and in time. Practically speaking, there is a bigger chance for the longer path to be influenced by disturbances. Though in developing the algorithm the Debye length effect is not taken into consideration, this effect does exist in the space environment. Thus, the shorter path with point D being the periapsis is preferred.

Finally, all the required substeps have been presented to outline the overall collision-avoidance algorithm. The basic logic is to search for a proper t_B^* such that the collision-avoidance criteria

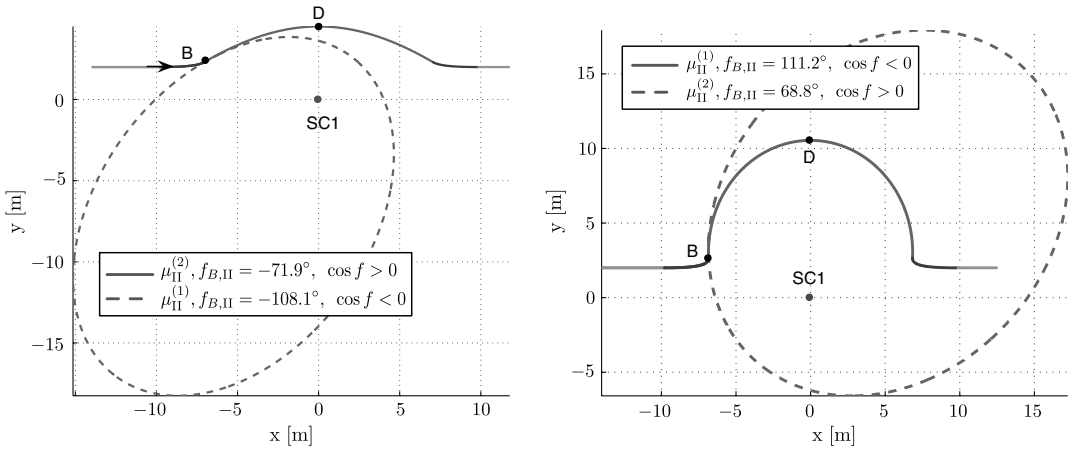

a) Point *D* is the periapsis of phase-II **b) Point *D* is the apoapsis of phase-II**

Fig. 4 Two cases of using $\mu_{\text{II}}^{(1,2)}$ solutions; in both cases, only one of the two solutions results in an actual symmetric trajectory.

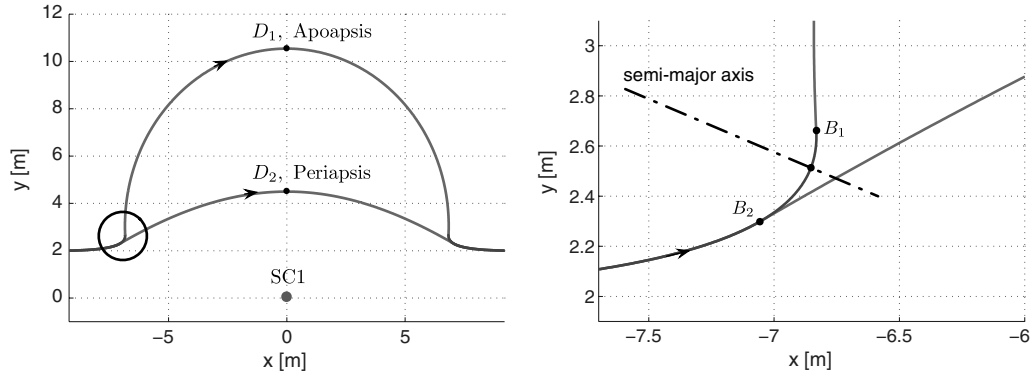

a) Big scenario **b) Focused on phase-I & phase-II connecting points**

Fig. 5 Illustration of the two cases with point D being the periapsis and apoapsis of phase II.

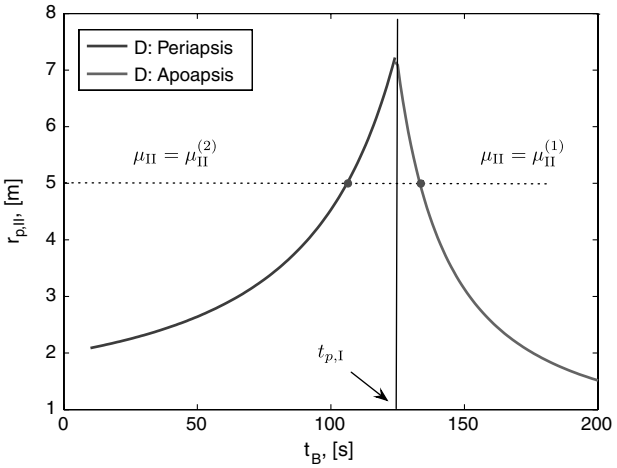

Fig. 6 Given $\mu_{\rm I}$, the resulting $r_{p,\rm II}$ with respect to t_B.

$$r_{p,\rm II} = \gamma r_s \tag{48}$$

is satisfied, with point D being the periapsis of phase II. In this paper, Newton's method is used in the numerical searching for t_B^* such that the following target function becomes zero:

$$g(t_B) = r_{p,\rm II}(t_B) - \gamma r_s \tag{49}$$

The iteration routine to determine a symmetric collision avoidance, with point D being the periapses of phase II propagates according to the following steps:

Step 1, initialization: From the measurements $\boldsymbol{r}_A$ and $\dot{\boldsymbol{r}}_A$, calculate $e_{\rm I}$ and $a_{\rm I}$ through Eq. (17), and calculate the angle $\angle AOD$ through Eq. (18). Prescribe a proper $\mu_{\rm I}$, which means that $|\mu_{\rm I}|$ must be greater than $|\mu_{\rm I,c}|$ to ensure $r_{p,\rm I} > \gamma r_s$. It must also make sure $Q_{\rm I}$ is implementable, which means $Q_{\rm I} < Q_{\max}$. Calculate $t_{p,\rm I}$. Initialize t_B:

$$t_B^{(0)} = \alpha t_{p,\rm I} \tag{50}$$

where $0 < \alpha < 1$.

Step 2: Solve for point B's states r_B and v_B through Eqs. (29–32).

Step 3: Solve for $\mu_{\rm II}^{(2)}$ by Eq. (44), using the minus sign. Calculate $r_{p,\rm II}$ through

$$r_{p,\rm II} = a_{\rm II}(1 - e_{\rm II}) \tag{51}$$

where $a_{\rm II}$ is solved by the energy equation, and $e_{\rm II}$ is calculated through Eq. (37) evaluating at point B in phase II.

Step 4: Calculate $g(t_B)$ by Eq. (49). Judge whether $|g(t_B)| < \text{tol}$. If yes, stop. Otherwise, go to step 5. Here, tol is the tolerance of the iteration error in the unit of meters. This paper uses $\text{tol} = 10^{-4}$ m in the numerical simulations.

Step 5: Calculate $g' = \partial g / \partial t_B$ using the finite difference method.

Step 6: Update $t_B^{(i+1)} = t_B^{(i)} - (g/g')$ $(i = i + 1)$. Go to step 2.

After choosing a proper value of $Q_{\rm I}$, this routine calculates a symmetric collision-avoidance trajectory composed of three patched conic sections.

V. Collision-Avoidance Criteria with Charge Saturation

The previous section develops a numerical routine to find a symmetric patched-conic-section trajectory to avoid the collision and meanwhile preserve the relative velocity magnitude and direction of the two-spacecraft system. In deriving this routine, it is assumed that the charge product of the two spacecraft is unlimited. If the charge-product limitation is taken into consideration, the system's ability to avoid a potential collision is then limited. Under certain conditions (for example, two spacecraft are approaching each other too quickly), the collision would be unpreventable. This section determines the criteria to predict whether a potential collision can be prevented using the presented collision-avoidance routines.

Figure 7 illustrates the geometry of the two-spacecraft system when the collision-avoidance strategy is triggered at time t_A. The vectors $\boldsymbol{r}_A$, $\boldsymbol{v}_A$, and $\boldsymbol{h}$ can be expressed in the $\{\hat{\imath}_v, \hat{\imath}_h, \hat{\imath}_D\}$[‡] frame as

$$\boldsymbol{r}_A = -x_A \hat{\imath}_v + d\hat{\imath}_D \tag{52a}$$

$$\boldsymbol{v}_A = v_0 \hat{\imath}_v \tag{52b}$$

$$\boldsymbol{h} = \boldsymbol{r}_A \times \boldsymbol{v}_A = d v_0 \hat{\imath}_h \tag{52c}$$

This section is investigating the critical state with $\gamma = 1$. Substituting Eq. (52) into Eq. (24) and using the fact $\|\boldsymbol{r}_A\| = r_\phi$ yield

$$\mu_{\rm I,c} = \frac{r_\phi v_0^2 d^2 - r_s^2 r_\phi v_0^2}{2 r_s (r_\phi - r_s)} \tag{53}$$

Equation (53) provides the value of $\mu_{\rm I}$ that results in $r_{p,\rm I} = r_s$. Thus, the circular transitional orbit solution gives $\mu_{\rm I}$ in the critical state.

Theorem 2. Consider a repulsive hyperbola motion governed by Eq. (7), with $\mu < 0$ being constant. Given initial position and velocity $[\boldsymbol{r}_0, \dot{\boldsymbol{r}}_0]$, the radius of the periapsis r_p increases as $|\mu|$ increases.

Proof. To mathematically prove this theorem, it is required to express r_p in terms of μ and initial conditions. For a repulsive hyperbola, the periapsis radius is given as [16]

$$r_p = a(1 + e) \tag{54}$$

[‡]The frame $\{\hat{\imath}_v, \hat{\imath}_h, \hat{\imath}_D\}$ centers at SC1, with $\hat{\imath}_v$ pointing to the SC2's relative velocity direction, $\hat{\imath}_h$ is the unit vector of the relative angular momentum, $\hat{\imath}_D$ closes the right-hand coordinate.

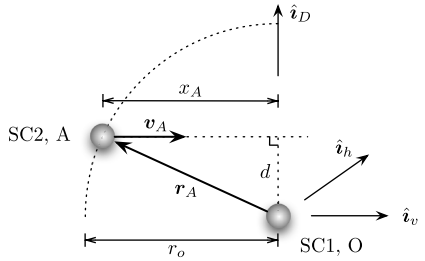

Fig. 7 Geometry of the two-spacecraft system.

where a and e are actually determined by the initial conditions and μ. Substituting $e = \sqrt{1 - h^2/\mu a}$ and Eq. (17b) into Eq. (54) and using $|\mu| = -\mu$ instead of μ yields

$$r_p = \frac{1}{2|\mu|/r_0 + v_0^2}\left(|\mu| + \sqrt{|\mu|^2 + h^2(2|\mu|/r_0 + v_0^2)}\right) \tag{55}$$

where $r_0 = \|\boldsymbol{r}_0\|$, $v_0 = \|\dot{\boldsymbol{r}}_0\|$, and $h = \|\boldsymbol{r}_0 \times \dot{\boldsymbol{r}}_0\|$, which are all determined by the initial conditions.

It is still not obvious to see the trend of r_p as $|\mu|$ increases. Taking a partial derivative of r_p with respect to $|\mu|$ yields

$$\frac{\partial r_p}{\partial|\mu|} = \frac{1 + (|\mu| + h^2/r_0)/\beta}{2|\mu|/r_0 + v_0^2} - \frac{|\mu| + \beta}{r_0(2|\mu|/r_0 + v_0^2)^2} \tag{56}$$

where

$$\beta = \sqrt{|\mu|^2 + h^2(2|\mu|/r_0 + v_0^2)}$$

The trend of r_p as μ increases is determined by the sign of $\partial r_p/\partial|\mu|$. Equation (56) can be changed to be

$$\frac{\partial r_p}{\partial|\mu|} = \frac{1}{(2|\mu|/r_0 + v_0^2)^2}\left\{\frac{|\mu|}{r_0} + v_0^2 + \left(\frac{|\mu|^2}{r_0} + |\mu|v_0^2\right)\Big/\beta\right\} \tag{57}$$

Equation (57) gives a simplified expression of $\partial r_p/\partial|\mu|$ with every individual term being positive. Thus, the partial derivative $\partial r_p/\partial|\mu|$ is always positive. This proves that r_p increases as $|\mu|$ increases. □

Applying Theorem 2 in the three-phase symmetric patched-conic-section scenario yields the following lemma.

Lemma 1. For the three-phase patched-conic-section scenario shown in Fig. 2, the circular transitional trajectory solution provides the minimum value of Q_{I} that satisfies the collision-avoidance constraint $r_{\min} \geq r_s$.

Proof. For the critical case in which $\gamma = 1$, the circular transitional trajectory has the following properties:

$$r_{p,\mathrm{I}} = r_s, \qquad r_{\mathrm{II}} = r_s \tag{58}$$

where r_{II} is the radius of phase II, which is constant.

By Theorem 2, $\mu_{\mathrm{I},c}$ in Eq. (53) provides the minimum value of $|\mu_{\mathrm{I}}|$ that satisfies $r_{p,\mathrm{I}} \geq r_s$. From Eq. (6), the charge product Q_{I} is proportional to $|\mu_{\mathrm{I}}|$; thus, the circular transitional trajectory provides the minimum value of Q_{I} such that $r_{p,\mathrm{I}} \geq r_s$. For phase II, the radius is equal to r_s, which satisfies the collision-avoidance requirement. So the circular transitional trajectory solution provides the minimum Q_{I} to avoid the collision. □

Theorem 3. For the two effective gravitational coefficients given by Eq. (24) and (25), $\mu_{\mathrm{I},c} > |\mu_{\mathrm{II},c}|$ if and only if

$$d < d^* = r_s\sqrt{\frac{r_\phi}{3r_\phi - 2r_s}}$$

Proof. First, let us investigate $\mu_{\mathrm{II},c} - |\mu_{\mathrm{I},c}|$:

$$\begin{aligned}\mu_{\mathrm{II},c} - |\mu_{\mathrm{I},c}| &= \mu_{\mathrm{II},c} + \mu_{\mathrm{I},c} = \frac{h^2}{r_s} + \frac{r_\phi v_0^2 d^2 - r_s^2 r_\phi v_0^2}{2r_s(r_\phi - r_s)} \\ &= \frac{v_0^2}{2r_s(r_\phi - r_s)}((3r_\phi - 2r_s)d^2 - r_\phi r_s^2)\end{aligned} \tag{59}$$

When $|\mu_{\mathrm{I},c}| > \mu_{\mathrm{II},c}$, then $\mu_{\mathrm{II},c} - |\mu_{\mathrm{I},c}| < 0$; applying this to the formula in Eq. (59) yields

$$\frac{v_0^2}{2r_s(r_\phi - r_s)}((3r_\phi - 2r_s)d^2 - r_\phi r_s^2) < 0 \Leftrightarrow d < \sqrt{\frac{r_\phi r_s^2}{3r_\phi - 2r_s}} = d^* \tag{60}$$

□

Theorem 2 and Lemma 1 show that Q_{I} is lower bounded by the circular phase II solution:

$$Q_{\mathrm{I}} \geq Q_{\mathrm{I},c} = -\frac{\mu_{\mathrm{I},c} m_1 m_2}{k_c(m_1 + m_2)} = -\frac{(r_\phi v_0^2 d^2 - r_s^2 r_\phi v_0^2)m_1 m_2}{2k_c r_s(r_\phi - r_s)(m_1 + m_2)} \tag{61}$$

If d satisfies the condition in Theorem 3, then the circular transfer orbit provides the minimum charge-product level among all the collision-avoidance solutions. To illustrate this, consider the following numerical simulation results with the initial conditions:

$$\begin{aligned}\boldsymbol{R}_1(t_0) &= [0, 0, 0]^T \text{ m}, & \dot{\boldsymbol{R}}_1(t_0) &= [0, 0, 0]^T \text{ m/s} \\ \boldsymbol{R}_2(t_0) &= [20, d, 0]^T \text{ m}, & \dot{\boldsymbol{R}}_2(t_0) &= [-0.03, 0, 0]^T \text{ m/s}\end{aligned} \tag{62}$$

and with $r_\phi = 15$ m and $r_s = 5$ m. Figure 8 shows the charge-product magnitudes under different values of the offset distance d. For the circular transitional trajectory case, Theorem 3 states that $Q_{\mathrm{I}} > Q_{\mathrm{II}}$ when $d < 3.2733$ m, and this is reflected in Fig. 8a. Because the minimum magnitude of Q_{I} is given by the circular

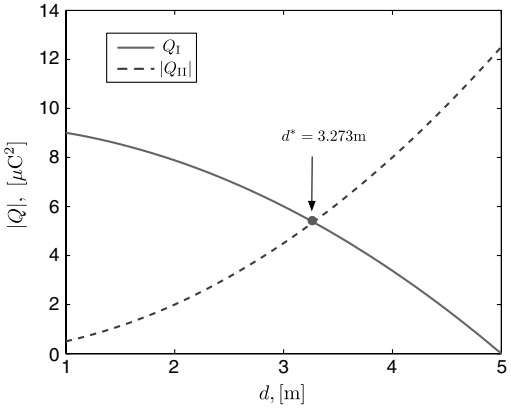

a) Circular transitional trajectory

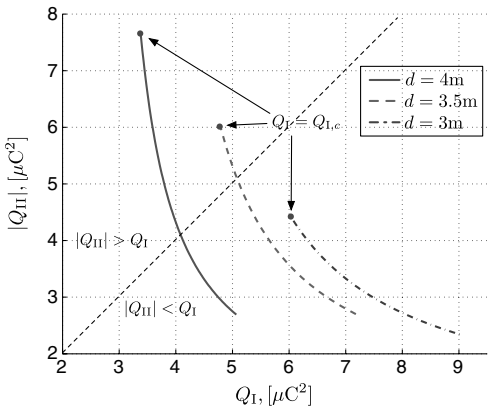

b) General symmetric trajectory solution, Q_{I}–Q_{II} plane

Fig. 8 Charge product values under different d.

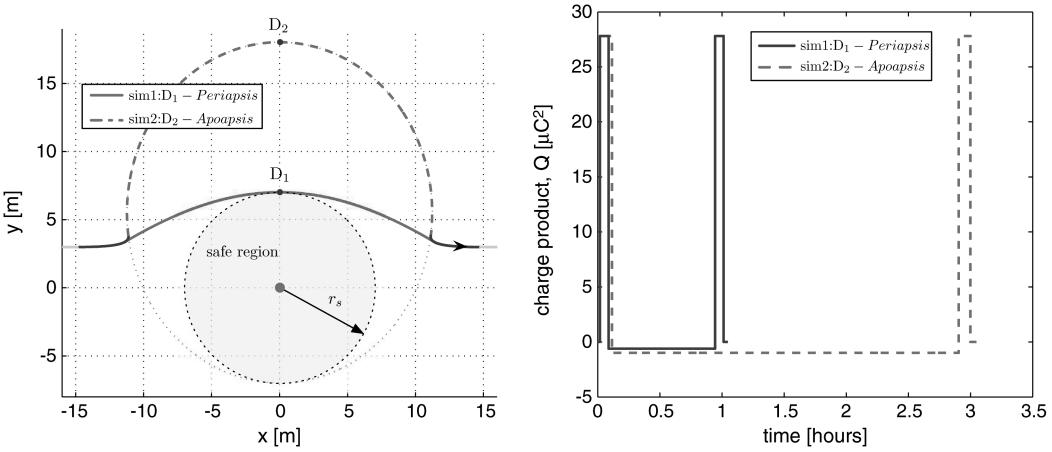

a) Relative trajectories **b) Charge product histories**

Fig. 9 Idea simulation.

transitional trajectory solution, the circular transitional trajectory solution gives the minimum charge product throughout the maneuver.

For general symmetric-trajectory cases, given a value of d, there remains one degree of freedom to determine the collision-avoidance trajectory. The numerical algorithm presented in the last section chooses a value of Q_{I} and calculates all the remaining variables. Figure 8b shows the value of $|Q_{\mathrm{II}}|$ corresponding to Q_{I} under different d, with all other variables the same as in Fig. 8a.

Figure 8b illustrates that the solution with $|Q_{\mathrm{II}}| < Q_{\mathrm{I}}$ always exists, whereas the solution with $|Q_{\mathrm{II}}| > Q_{\mathrm{I}}$ exists only when $d > d^*$. This agrees with the intuition that Q_{I} can be infinitely large to achieve the symmetric collision-avoidance trajectory, but it must be greater than a certain value to ensure a collision avoidance with $r > r_s$. When $d < d^*$, the minimum acceptable value of Q_{I} is still greater than corresponding $|Q_{\mathrm{II}}|$, as predicted by Theorem 3; thus, the solution with $|Q_{\mathrm{II}}| > Q_{\mathrm{I}}$ does not exist in this situation. Another important aspect is that if $d < d^*$, the solution with $Q_{\mathrm{I}} = |Q_{\mathrm{II}}|$ is the L_∞ charge-optimal solution; when $d > d^*$, the circular transfer orbit is the L_∞ charge-optimal solution. This helps to choose a proper value of Q_{I} such that the maximum charge level during the whole process is minimized.

Note that the criterion in Eq. (61) has exactly the same form as Eq. 42 in [15]. The authors of [15] assume that the two spacecraft are fully charged to get the criteria in Eq. 42 in [15]. This assumption matches with the situation in phase I, where the two spacecraft have a constant charge product and are repelling each other. The physical meanings of the criteria in Eq. 42 in [15] can be used here. For a given formation-flying mission in which the maximum magnitude of the possible separation distance rate has been determined, Eq. (61) provides a guide to design the spacecraft charge devices such that $Q_{\mathrm{I},c}$ is achievable; thus, the collision can be avoided with a symmetric trajectory.

If the maximum charge product has been specified, then Eq. (63) tells us the maximum allowable relative velocity that guarantees the collision to be avoidable:

$$v_0 \le \sqrt{\frac{2Q_{\mathrm{I,max}}k_c(m_1+m_2)}{m_1m_2}\frac{r_s(r_\phi - r_s)}{r_\phi(d^2-r_s^2)}} \tag{63}$$

Note that the inequality in Eq. (63) is obtained by solving for v_0 from the inequality in Eq. (61).

VI. Numerical Simulations

A numerical iteration routine using Newton's method to solve for a symmetric patched-conic-section trajectory has been set up. The logic of the routine is to search an appropriate time value t_B such that the target function $g(t_B)$ defined in Eq. (49) converges to zero, with point D being the periapsis of phase II.

The following numerical simulation cases show the effectiveness of the routine in different situations. All the cases share a common set of the parameters of the two-spacecraft system:

$$m_1 = m_2 = 50 \text{ kg}, \qquad r_\phi = 15 \text{ m}, \qquad r_s = 7 \text{ m}, \qquad \gamma = 1 \tag{64}$$

The initial inertial state vectors are also the same across all numerical studies unless specified:

$$\begin{cases} \boldsymbol{R}_1(t_0) = [0,0,0]^T \text{ m} \\ \boldsymbol{R}_2(t_0) = [-16,3,0]^T \text{ m} \end{cases} \qquad \begin{cases} \dot{\boldsymbol{R}}_1(t_0) = [0,0,0]^T \text{ m/s} \\ \dot{\boldsymbol{R}}_2(t_0) = [0.02,0,0]^T \text{ m/s} \end{cases} \tag{65}$$

The numerical simulation integrates the fundamental equations of motion (4) using a variable-step-size fourth-order Runge–Kutta integrator.

A. Ideal-Condition Examples

The phrase *ideal conditions* means that the two spacecraft are flying in free space in a vacuum (no plasma environment) with $\lambda_d = \infty$. Setting the variable $\mu_{\mathrm{I}} = -0.01 \text{ m}^3/\text{s}^2$, the corresponding charge product is $Q_{\mathrm{I}} = 27.81 \ (\mu\text{C})^2$. Figure 9 shows two simulation results under these conditions. The first trajectory (solid line) has point D as the periapsis of phase II. The second trajectory (dashed line) is the case in which point D is the apoapsis of phase II. This can be achieved by initializing t_B to be larger than $t_{p,\mathrm{I}}$ and by using $\mu_{\mathrm{II}}^{(1)}$ instead of $\mu_{\mathrm{II}}^{(2)}$ in the routine. Table 1 shows some detailed results of the simulations.

In both of the two simulations, the collision-avoidance requirement $r_{\min} \ge r_s$ is satisfied and the final relative-speed direction is held the same as the initial direction. The first simulation has the shorter path, though the magnitude of Q_{II} is bigger. The apoapsis case (point D is the apoapsis of phase II) is a conservative trajectory far exceeding the collision-avoidance requirement. Notice that a small difference in t_B results in a huge difference in the total maneuver time. The longer transition time span makes the apoapsis case much more vulnerable to disturbances.

B. Charge-Expense Analysis

In these simulations, the charge expense under different choices of the free variable μ_{I} is analyzed. Two charge cost functions are defined as

Table 1 Results of the ideal simulations

	t_B, s	r_D, m	Q_{II}, μC^2
sim 1	291.42	7.00	−6.480
sim 2	391.61	15.64	−1.036

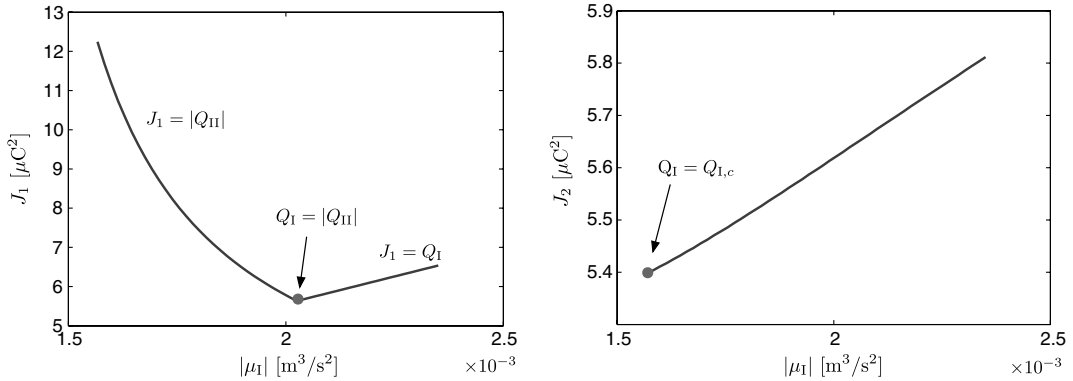

a) Maximum charge product magnitude **b) Time averaged charge product**

Fig. 10 Charge expense history while sweeping $\mu_{\rm I}$.

$$J_1 = \max(Q_{\rm I}, |Q_{\rm II}|), \qquad J_2 = \frac{2t_B Q_{\rm I} + t_{\rm II}|Q_{\rm II}|}{2t_B + t_{\rm II}} \tag{66}$$

where J_1 is the maximum magnitude of the charge products. This is important when the maximum vehicle voltage level is of concern. J_2 is the time averaged charge product, which provides insight into the nominal charge and voltages levels. Numerical sweeps of $|\mu_{\rm I}|$ are performed using the same parameters as in Eq. (64) but with different initial conditions:

$$\begin{cases} \boldsymbol{R}_1(t_0) = [0,0,0]^T \text{ m} \\ \boldsymbol{R}_2(t_0) = [-16,6,0]^T \text{ m} \end{cases}, \quad \begin{cases} \dot{\boldsymbol{R}}_1(t_0) = [0,0,0]^T \text{ m/s} \\ \dot{\boldsymbol{R}}_2(t_0) = [0.03,0,0]^T \text{ m/s} \end{cases} \tag{67}$$

Note that with the provided parameters and initial conditions, the condition in Theorem 3 is not satisfied, which implies that the solution with $|Q_{\rm II}| > Q_{\rm I}$ exists. Figure 10 shows the values of J_1 and J_2 for each value of $|\mu_{\rm I}|$. Figure 10a shows that the minimum value of J_1 is achieved at the marked point at which $Q_{\rm I} = |Q_{\rm II}|$. As $|\mu_{\rm I}|$ increases, before it reaches point at which $|Q_{\rm II}| = Q_{\rm I}$, $|Q_{\rm II}|$ dominates and $J_1 = |Q_{\rm II}|$. After the marked point, J_1 is linearly increasing, because now $J_1 = Q_{\rm I}$ and $Q_{\rm I}$ is proportional to $|\mu_{\rm I}|$. Figure 10b shows that the minimum J_2 happens at the point at which $Q_{\rm I}$ is minimum. This is because when $Q_{\rm I} = Q_{1,c}$, $2t_B$ is about two times greater than $t_{\rm II}$, and as $|\mu_{\rm I}|$ increases, t_B is increasing and $t_{\rm II}$ is decreasing. So the influence of t_B dominates J_2. Thus, $J_2 \approx Q_{\rm I}$, as shown in Fig. 10b.

The two plots in Fig. 10 together show an example that, according to difference charge expense concerns, the optimal solutions can be different.

C. Simulation with Debye Length Effect

The algorithm developed in this paper is an open-loop programming algorithm, assuming that the spacecraft are flying in free space. The orbital motion and the Debye shielding effect have not been taken into account. Figure 11 compares an ideal trajectory (dashed line) with a trajectory in the presence of the Debye shielding (solid line) under the same initial conditions. In the case in which the Debye shielding is applied, the Debye length is set to be $\lambda_d = 50$ m. This value represents the Debye length in deep space at 1 AU distance from the sun.

The final velocity direction of the disturbed trajectory has an offset of 3.98° from the ideal trajectory. The minimum distance of the disturbed trajectory is 0.254 m, or about 3.6% less than that of the ideal case γr_s, due to the partial shielding of coulomb force. The Debye length always decreases the effectiveness of the coulomb repulsion. This effect could be compensated for with a $\gamma > 1$ safety factor. Future work will investigate how to feedback-stabilize such open-loop trajectories. A challenge here is the underactuated nature of the coulomb thrusting. Further, the momentum conservation makes it impossible to reverse the motion to compensate for an overshoot. Any feedback-control development could try to bias the tracking errors to slightly undershoot the desired trajectory.

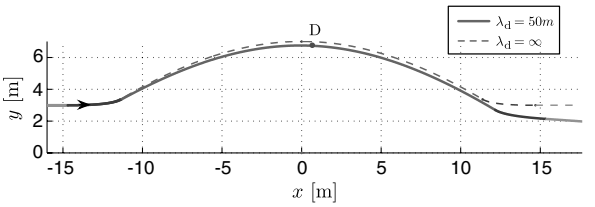

Fig. 11 Relative trajectories of the two spacecraft under the condition $\lambda_d = 50$ m.

VII. Conclusions

This paper proposes a symmetric three-phase relative trajectory composed of patched conic sections as the collision-avoidance trajectory. An analytical solution to circular transitional symmetric trajectory and a numerical routine to find general symmetric-trajectory solutions are developed. With the presence of the Debye shielding effect, the trajectory deviates from the ideal trajectory, but only with small errors of a few percent. An issue in generating the algorithm for a multiple-spacecraft formation is that increasing the number of the spacecraft would rapidly increase the complexity of the problem. But the control algorithm in this paper can be applied in a multispacecraft formation in the case in which two spacecraft are very close and others are far away from these two spacecraft. In this case, the impact from other spacecraft can be treated as disturbances. The study of the impact from other spacecraft in a formation is one direction for further study. The results in this paper can be extended to more general applications such as an asymmetric flyby maneuver. The final relative velocity's direction can be controlled by changing the symmetric axis. The magnitude of the final relative velocity can be controlled by changing the energy level of phase III; correspondingly, the properties of the phase III trajectory are also changed and need to be treated carefully.

References

[1] Patera, R. P., and Peterson, G. E., "Space Vehicle Maneuver Method to Lower Collision Risk to an Acceptable Level," *Journal of Guidance, Control, and Dynamics*, Vol. 26, March–April 2003, pp. 233–237. doi:10.2514/2.5063

[2] Slater, G. L., Byram, S. M., and Williams, T. W., "Collision Avoidance for Satellites in Formation Flight," *Journal of Guidance, Control, and Dynamics*, Vol. 29, Sept.–Oct. 2006, pp. 1140–1146. doi:10.2514/1.16812

[3] Patera, R. P., "Space Vehicle Conflict-Avoidance Analysis," *Journal of Guidance, Control, and Dynamics*, Vol. 30, March–April 2007, pp. 492–498. doi:10.2514/1.24067

[4] King, L. B., Parker, G. G., Deshmukh, S., and Chong, J.-H., "Spacecraft Formation-Flying Using Inter-Vehicle Coulomb Forces," NASA Institute for Advanced Concepts, Atlanta, Jan. 2002, http://www.niac.usra.edu/files/studies/final_report/601King.pdf [retrieved 2009].

[5] Torkar, K., Riedler, W., and Escoubet, C. P., "Active Spacecraft Potential Control for Cluster Implementation and First Results," *Annales Geophysicae*, Vol. 19, Nos. 10–12, 2001, pp. 1289–1302.

[6] Torkar, K., Riedler, W., Fehringer, M., Rudenauer, F., Escoubet, C. P., Arends, H., Narheim, B. T., Svenes, K., McCarthy, M. P., Parks, G. K., Lin, R. P., and Reme, H., "Spacecraft Potential Control Aboard Equator-S as a Test for Cluster-II," *Annales Geophysicae*, Vol. 17, No. 12, 1999, pp. 1582–1591. doi:10.1007/s00585-999-1582-3

[7] Nishikawa, K., and Wakatani, M., *Plasma Physics Basic Theory with Fusion Applications*, 2nd ed., Springer, New York, 2000, pp. 56–60.

[8] Gurnett, D. A., and Bhattacharjee, A., *Introduction to Plasma Physics with Space and Laboratory Applications*, Cambridge Univ. Press, New York, 2005, pp. 7–9.

[9] Romanelli, C. C., Natarajan, A., Schaub, H., Parker, G. G., and King, L. B., "Coulomb Spacecraft Voltage Study Due to Differential Orbital Perturbations," *Advances in the Astronautical Sciences*, Vol. 124, 2006, pp. 361–380; also American Astronautical Society Paper AAS 06-123.

[10] Lappas, V., Saaj, C., Richie, D., Peck, M., Streeman, B., and Schaub, H., "Spacecraft Formation Flying and Reconfiguration with Electrostatic Forces," *Advances in the Astronautical Sciences*, Vol. 127, 2007, pp. 217–226American Astronautical Society Paper AAS 07-113.

[11] Schaub, H., and Hussein, I. I., "Stability and Reconfiguration Analysis of a Circulary Spinning 2-Craft Coulomb Tether," *IEEE Aerospace Conference*, Inst. of Electrical and Electronics Engineers, Paper 1361, March 2007.

[12] Vasavada, H., and Schaub, H., "Analytic Solutions for Equal Mass Four-Craft Static Coulomb Formation," *Journal of the Astronautical Sciences*, Vol. 56, Jan.–March 2008, pp. 7–40.

[13] Wang, S., and Schaub, H., "1-D Constrained Coulomb Structure Stabilization with Charge Saturation," *Advances in the Astronautical Sciences*, Vol. 129, 2007, pp. 257–274; also American Astronautical Society Paper AAS 07-267, Aug. 2007.

[14] Hussein, I. I., and Schaub, H., "Stability and Control of Relative Equilibria for the Three Spacecraft Coulomb Tether Problem," *Acta Astronautica*, Vol. 65, No. 5–6, 2009, pp. 738–754. doi:10.1016/j.actaastro.2009.03.035

[15] Wang, S., and Schaub, H., "Spacecraft Collision Avoidance Using Coulomb Forces with Separation Distance and Rate Feedback," *Journal of Guidance, Control, and Dynamics*, Vol. 31, May–June 2008, pp. 740–750. doi:10.2514/1.29634

[16] Hussein, I. I., and Schaub, H., "Invariant Shape Solutions of the Spinning Three Craft Coulomb Tether Problem," *Celestial Mechanics and Dynamical Astronomy*, Vol. 96, Oct. 2006, pp. 137–157. doi:10.1007/s10569-006-9043-8

[17] Bittencourt, J. A., *Fundamentals of Plasma Physics*, Springer–Verlag, New York, 2004, pp. 273–278.

[18] Schaub, H., Parker, G. G., and King, L. B., "Challenges and Prospect of Coulomb Formations," *Journal of the Astronautical Sciences*, Vol. 52, Jan.–June 2004, pp. 169–193.

[19] Pollock, G. E., Gangestad, J. W., and Longuski, J. M., "Charged Spacecraft Formations: A Trade Study On coulomb And Lorentz Forces," AAS/AIAA Spaceflight Mechanics Meeting, Pittsburgh, PA, American Astronautical Society Paper 09-389, Aug. 2009.

[20] Schaub, H., and Junkins, J. L., *Analytical Mechanics of Space Systems*, AIAA Education Series, AIAA, Reston, VA, Oct. 2003, pp. 404–408.